ACTA PHYSICA POLONICA A No. 4 Vol. **142** (2022)

Structural, Magneto-Resistivity and Magnetization Investigations of $Y(Ba_{1-x}Mg_x)_2Cu_3O_{7-\delta}$ Superconducting System

Ö. Çiçek* and K. Yakinci

Department of Basic Engineering Sciences, Faculty of Engineering and Natural Sciences, İskenderun Technical University, 31200, İskenderun/Hatay, Turkey

Received: 12.04.2022 & Accepted: 26.09.2022

Doi: 10.12693/APhysPolA.142.478

*e-mail: ozlemthecicek@yahoo.com

In this study, YBCO superconducting samples with the nominal composition of $Y(Ba_{1-x}Mg_x)_2Cu_3O_{7-\delta}$, where $x = 0.0$, 0.5, 1.0, and 1.5, were prepared by the solid-state method to get better superconducting properties. Structural, electrical transport, and magnetic characterizations up to ±9 T applied fields were performed, including calculations of the upper critical field $H_{c2}(0)$, irreversibility field $\mu_0 H_{irr}$, activation energy $U_0(J,\ T,H)$, and pinning force F_p, and the obtained results were presented the first time for the Mg substitution to a Ba site in an optimally-doped YBCO superconducting system. It was found that the crystal parameters changed with the Mg substitution, but the crystal symmetry remained unchanged. Two impurity phases, Y-211 and MgO, were grown and became dominant at high substitution ratios. The superconducting properties of the samples deteriorated with the substitution of Mg; even high MgO substituted samples showed no superconducting properties. Deteriorations were also obtained in the properties $H_{c2}(0)$, $\mu_0 H_{irr}$, $U_0(J,\ T,H)$, and F_p. Two important points are thought to be responsible for these deteriorations. (i) MgO is not being able to be fully resolved in the matrix. Therefore, instead of Mg replacing with Ba, MgO remains in the impurity phase. As a result of this, the Ba concentration in the structure gradually decreases, and then the superconductivity is destroyed. (ii) The samples shift from the optimally doped region to the over-doped region due to the increase in hole concentration.

topics: YBCO superconductors, activation energy, upper critical field, irreversibility field

1. Introduction

$YBa_2Cu_3O_{7-x}$ (Y-123) high-temperature superconductors (HTS), which have a history of around 30 years, are still up-to-date for technological applications as they show a superconducting transition, T_c, above the liquid nitrogen temperature. In addition, these materials show high current carrying capacities even under high magnetic fields, high values of the upper critical field $H_{c2}(0)$, easy production in the form of thin/thick films, tapes, and wires, and do not contain toxic elements. In order to carry a higher critical current and have smaller anisotropy, defects of various sizes and shapes and partial substitution/displacement studies were carried out on the Y-123 material [1–12]. The material Y-123 has a multilayer perovskite structure with oxygen deficiency and orthorhombic P/mmm symmetry. It also has Cu–O chains along the b-axis and two Cu–O layers in the ab-plane of the multilayer structure. In this context, the critical current density, J_c, of the system is strongly dependent on the Cu chains in the Cu–O planes, which control the carrier density, and thus the T_c value [13, 14]. Therefore, it was shown that positive results in terms of electrical transport could not be achieved in experimental studies using different elements for the Cu region.

However, it is an accepted idea that changes in characteristic parameters can be obtained by substituting any cation, particularly for the Y and/or Ba atoms in the system [15–16]. For example, it has been reported that the basic characteristics of Y-123 can be improved significantly with Er/Y partial substitution up to a certain level, but above this level, there is a dramatic deterioration due to the solid-solubility limit being exceeded [17].

It was confirmed by Shakeripour et al. [15] that the partial increase in T_c was achieved by the addition of magnetic elements such as Co, Fe, and Ni to the Y positions. Similarly, the substitutions Ce and Gd were studied for the Ba position in the Y-123 system, and although there is a decrease in T_c for both types of substitutions, an improvement in J_c

was reported for Ce-doped samples and deterioration for Gd-doped samples [16]. Another study revealed several types of pinning centers that increase J_c for substituting Mo to the positions of Cu atoms with extra oxygen treatment [18].

There are few studies in the literature on the substitution of Mg in the Y-123 structure, and all of them have been done for the Cu sites, however, there was no significant improvement obtained, especially in T_c values. For example, the effects of the double substitution of Y by Ca and Cu by Mg have been studied in polycrystalline $YBa_2Cu_3O_{7-\delta}$. It was found that the substitution of Ca alone reduces T_c and increases the width of the transition. The low rate of Mg substitution also reduced T_c more, and the width of the transition increased. However, a higher rate of Mg results in a decrease in the width of the transition. In addition, substitution with Ca alone reduces J_c, and substituting by Mg together with Ca seems to have a compensatory effect that enhances J_c and leads to values higher than in the undoped sample [19]. Vieira et al. [20] worked on the low field resistive transition, fluctuation conductivity, and magnetic irreversibility for fields applied along the c-axis as well as along the ab-plane of the $YBa_2Cu_2O_{7-\delta}$ single crystal sample in which 1 at.% of Cu was substituted by Mg. As reported, Mg impurities impede full oxygenation of the samples, a drastic decrease of T_c, and the growth of the effect of granularity in the sample [20]. Melt-textured single domains of Mg-doped $YBa_2(Cu_{1-x}Mg_x)_3O_7$ superconductors were prepared by top seeding growth by J. Figueras et al. [21]. They obtained a strong reduction in the T_c values of the samples. Their investigations also showed that the mass anisotropy decreased with Mg doping. They interpreted their results in the framework of the non-magnetic impurity scattering effects in d-wave superconductors, where the main distinguishing feature has been the development of new quasi-particle states within the superconducting gap [21]. The superconducting properties of $YBa_2(Cu_{1-x}Mg_x)_3O_{7-\delta}$ have also been studied by Raffo et al. [22], and they showed that an increase of the dopant content induces a contraction of the crystallographic c-axis and a reduction in T_c. They also reported that the Mg substitution affects the temperature dependence of J_c [22]. In another work [23], the relationship between pseudogap behavior and Mg doping was investigated, and it was reported that the magnitude of pseudo-gap increased with the level of Mg doping. In addition, it was found that the T_c value decreased with increasing Mg concentration in the structure [23]. Generally, the reason why Mg substitution is preferred for the Cu positions is due to the reduced ionic radius (0.65Å), which is close to the reduced ionic radius of Cu ions (0.72Å).

The sensitivity of Y-123 to the magnetic field due to its granular feature causes different results, especially in measurements made under a magnetic field. In order to explain the formation, movement, or freezing of pinning centers and the mechanism of vortex trapping, enlargement in ΔT $(= T_c - T_{\text{zero}})$ under the applied field should not be too extreme. Thus, it is more appropriate to evaluate the results with the thermally assisted Flux Flow (TAFF) mechanism and collective pinning theory (CPT) [4, 22–32], which can be successfully applied in HTS systems.

In this study, different proportions of Mg were substituted to the Ba site according to the formula $Y(Ba_{1-x}Mg_x)_2Cu_3O_{7-\delta}$, and results are presented.

2. Experimental methods

YBCO superconducting samples with a nominal composition $Y(Ba_{1-x}Mg_x)_2Cu_3O_{7-\delta}$, where x =0.0 0.5, 1.0, and 1.5, were prepared using the solid-state method. In the sample preparation stage, high purity (99.9%) Y_2O_3, $BaCaO_3$, CuO, and MgO (Alfa Aesar) powders were weighed in the determined stoichiometry as starting chemicals and mixed in an agate mortar for 60 min. The powder mixtures were then calcined for 12 h in air at 700 and 750°C. Between each calcination process, the powders were ground in an agate mortar for 60 min. Then, the powders were turned into pellet form under a pressure of 12 MPa and heated to 910°C with a heating rate of 5°C/min in an O_2 atmosphere for 24 h. Next, the samples were cooled down to room temperature with a cooling rate of 5°C/min. At the last stage, after taking the samples out of the furnace, they were ground in an agate mortar for 30 min and made into pellets, and then subjected to heat treatment again under the same conditions.

The characterization process of the prepared samples started with X-ray diffraction (XRD) analyses. In order to determine the phases and parameters of the crystal structure of the samples, the Cu K_α radiation and Malvern Panalytical Empyrean X-ray diffractometer were used in the range of $2\theta = 10$–$65°$, with a scan speed of 2°/min. The XRD patterns were then analyzed with the aid of the FullProf program and the phase analyses, and crystal structure parameters were solved.

For scanning electron microscope (SEM) analysis, the Thermo Scientific-FEI Apreo S system was used for surface morphology and phase analysis of the produced samples, and the energy-dispersive X-ray (EDS) detector, UltraDry EDS, and the electron backscatter diffraction (EBSD) detector, Quasor II EBSD, systems were used for stoichiometric analysis.

In order to determine the electrical transport properties, the magneto-resistance versus temperature measurements were carried out with up to 9 T applied field, parallel to the sample surface, and zero-field-cooling (ZFC) procedure. For all electrical measurements, rectangular bar-shaped samples with $1 \times 1.5 \times 10$ mm^3 in size and physical property measurement system (PPMS),

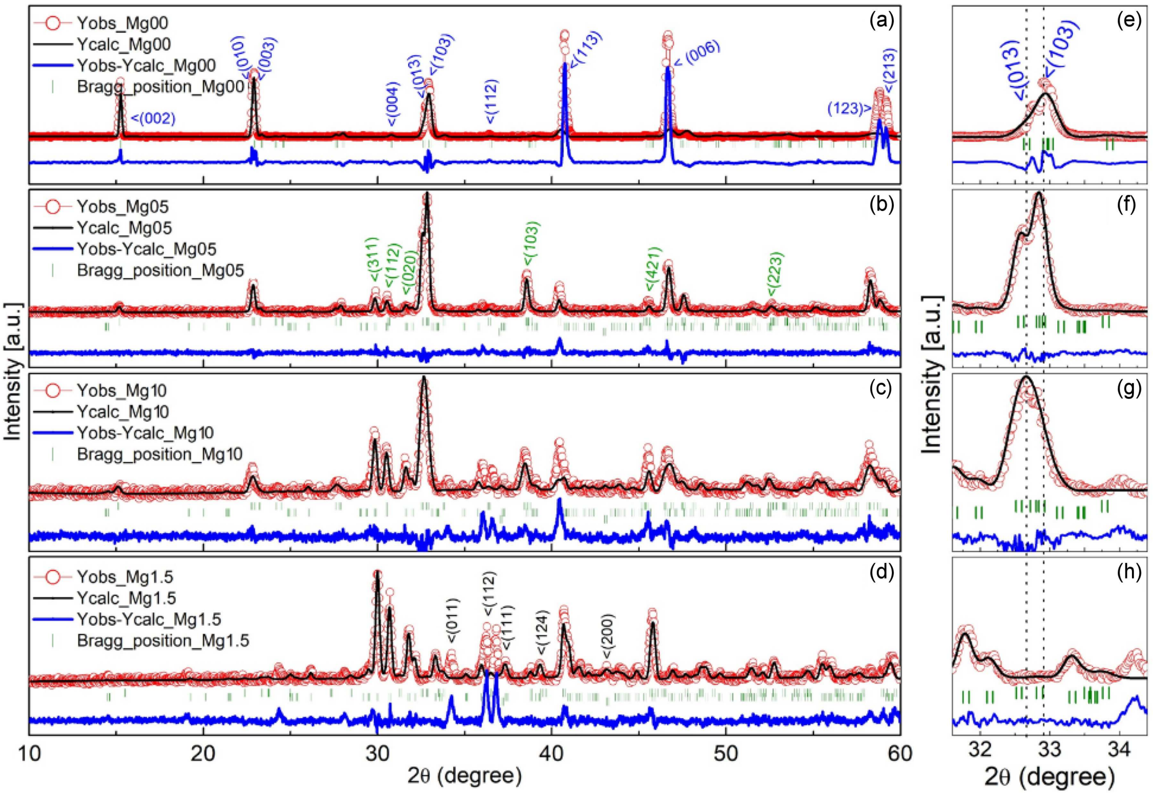

Fig. 1. XRD patterns and Rietveld refinement results of (a) Pure, (b) Mg05, (c) Mg10, and (d) Mg15 samples prepared. Panels (e–h) show changes on the twin characteristic peak at $2\theta = 32.536/32.893$ for Pure, Mg05, Mg10 and Mg15 samples, respectively. Blue numbers show Y-123 phase planes, green number show Y-211 phase planes and black numbers indicates MgO phase planes.

Quantum Design PPMS-9T, was used. Magnetic properties were determined by Quantum Design vibrating sample magnetometer (VSM) attachment, fixed to the PPMS-9T system. Magnetization-temperature measurements (M–T) and magnetization-applied field ($M - -H$) analyzes were carried out with $1 \times 1.5 \times 10$ mm^3 in size rectangular bar-shaped samples and ±9 T applied magnetic fields parallel to the sample surface. In order to make following the samples throughout the text easier, the pure sample is coded as Pure, $\mathrm{Y(Ba_{1.5}Mg_{0.5})_2Cu_3O_{7-\delta}}$ sample as Mg05, $\mathrm{Y(Ba_{1.0}Mg_{1.0})_2Cu_3O_{7-\delta}}$ sample as Mg10, and $\mathrm{Y(Ba_{0.5}Mg_{1.5})_2Cu_3O_{7-\delta}}$ sample as Mg15.

3. Results and discussions

3.1. XRD analysis

The XRD patterns and Rietveld refinement results of the produced samples in this work are given in Fig. 1a–h. No impurity phase was found in the Pure sample, and characteristic 013/103 twin peaks of the Y-123 material were obtained at $2\theta = 32.53/32.89$ (Fig. 1a). In Fig. 1b, the XRD pattern of the Mg05 sample is given. As seen from the pattern, especially of the $\mathrm{Y_2Ba_1Cu_1O_x}$, the Y-211 phase has started to form in the matrix, and along with this, the intensities of the main phase peaks, except the 013/103 peaks of the Y-123 phase, have begun to decrease. In the Mg10 sample, a more complex situation was encountered compared to the Mg05. Together with the Y-211 phase, the MgO phase started to form as an additional impurity. Also, the cleavage in the 013/103 characteristic twin peak disappears, and their intensities equalize and return to a single peak form (Fig. 1c and Fig. 1e–h). When the substitution ratio was further increased to Mg15, the Y-123 phase began to be suppressed by the Y-211 and MgO phases, and the structure was transformed into a highly complex multiphase matrix form (Fig. 1d). As seen in Fig. 1h, 013/103 characteristic twin peak disappeared completely, implying that the fraction of the Y-123 phase significantly decreased in the Mg15 sample.

The structural parameters, including atomic positions, were obtained from the Rietveld refinement. To refine the main Y-123 phase, it was assumed that all occupancies were 1 for all the sites — Y $(1/2, 1/2, 1/2)$; Ba $(1/2, 1/2, z)$; $\mathrm{Cu_1}$ $(0, 0, 0)$; $\mathrm{Cu_2}$ $(0, 0, z)$; $\mathrm{O_1}$ $(0, 0, z)$; $\mathrm{O_2}$ $(1/2, 0, z)$; $\mathrm{O_3}$ $(0, 1/2, z)$; $\mathrm{O_4}$ $(0, 1/2, 0)$ — for the initial refinements. We consider χ^2 of the refinement to be the main sign of the beneficence of fitting. A single Y-123 phase improvement was conducted until χ^2 remained constant. Then, the Y-211 phase and MgO phase were added

TABLE I

Rietveld refinement results of the samples. 1538678 file is available in Crystallography Open Data Base COD [33].

Properties	COD ID: 1538678	Pure (χ^2: 4.67)	Mg05 (χ^2: 1.44)	Mg10 (χ^2: 1.78)	Mg15 (χ^2: 3.45)
a-axis [Å]	3.8200	3.8120(5)	3.8224(5)	3.8369(6)	3.8499(6)
b-axis [Å]	3.8800	3.8810(6)	3.8874(5)	3.8827(5)	3.8861(6)
c-axis [Å]	11.6620	11.6300(4)	11.6672(5)	11.7016(5)	11.8384(5)
Cell V. [Å^3]	172.85	171.8709	173.125	174.3250	170.432
Fraction of Y-123 [%]	–	100.00	95.40	82.48	48.56
c/a	3.0492	3.0509	3.0523	3.0498	3.0750
c/b	2.9893	2.9967	3.0013	3.0138	3.0463
Ortho-rhombicity $(b-a)/(b+a)$	0.0099	0.0090	0.0084	0.0059	0.0047

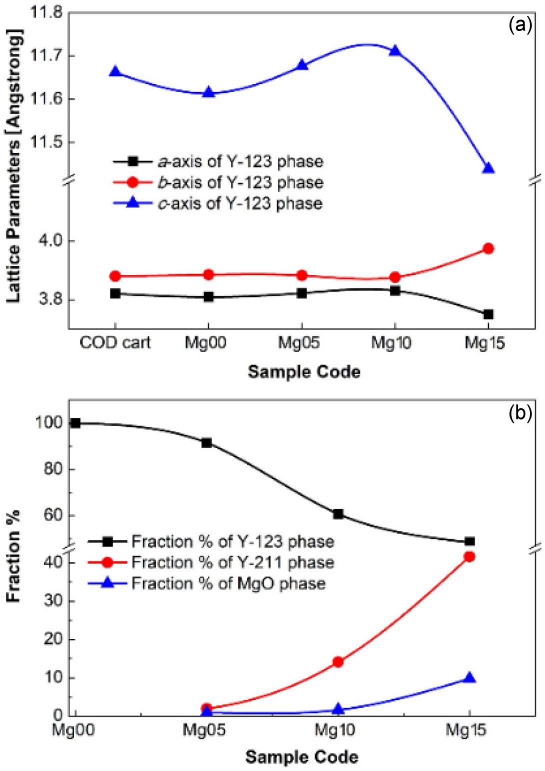

Fig. 2. (a) Calculated lattice parameters and (b) phase fraction of the samples prepared.

to this refinement work. The structural parameters for the samples were refined, and the calculated values of the fittings agreed well with the observed spectrum, Fig. 1a–d. In accordance with XRD patterns and the Rietveld analyses, it was found that the crystal structure is in the orthorhombic form, and the space group is *Pmmm*. This is confirmed by the presence of characteristic discrete 013/103 peaks [34, 35].

Figure 2a and b show the lattice parameters change and phase fractions, respectively. When the Mg concentration increased, there was an increase in the a-axis, no significant change in the b-axis, and a systematic increase in the c-axis (Fig. 2a and Table I). With the increase in the substitution ratio in the matrix, it was seen that the orthorhombicity value and crystallite sizes decreased significantly. According to the Rietveld analysis, there is no orthorhombic–tetragonal phase transformation obtained, and, in addition, it is clearly seen that the Y-123 fraction decreased with increasing substitution ratio, while the Y-211 and MgO phases increased (Table I and Fig. 2b). According to these data, the absence of large displacement in the characteristic XRD peaks of Y-123 and the prominent appearance of the peaks of the MgO phase reveal that Mg did not enter the crystal structure fully and did not fully react with the Y-123 material itself. However, we assume that Mg may have reacted with Y-123 at an atomic size at a certain rate, as much as the solid-solubility allows, and Ba deficiency in the structure may cause dislocations in different formats and affect the crystal parameters. In addition, the fact that the c/a and c/b ratios change slightly with increasing the amount of Mg substitution shows that there is a certain amount of internal lattice strain in the structure, and we believe that Mg is concentrated mostly in the intergranular region.

3.2. SEM and EDS analysis

The surface morphologies of the prepared samples are given in Fig. 3a–e. For the Pure sample (Fig. 3a), it was observed that there was a partial melting and particles of different sizes and geometries on the surface of the samples. This actually delineates the classical structure of the Y-123 bulk material obtained previously by various research groups [36–38]. Similar morphology was obtained in the Mg05 sample, and it was found that partial melting continued, and rectangular and spherical particles ranging from 1–15 μm in size formed on the partly molten surfaces (Fig. 3b). As a result of the EDS analysis, it was found that these spherical-shaped particles mainly represent the Y-211 phase. In Fig. 3c, a surface micrograph of the Mg10 sample

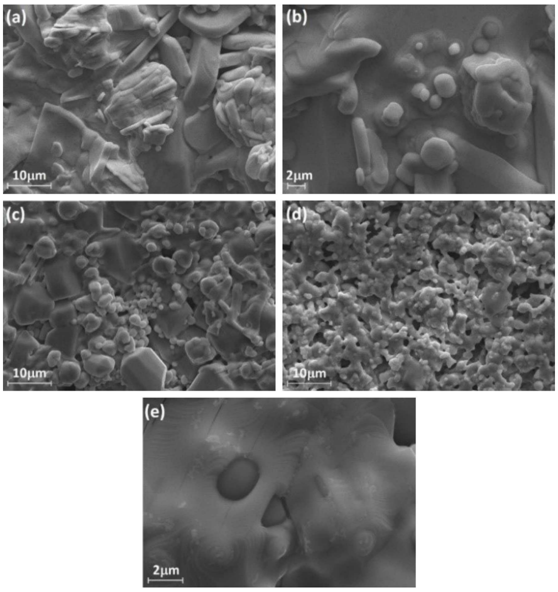

Fig. 3. SEM micrographs of (a) Pure sample, (b) Mg05 sample, (c) Mg10 sample, (d) Mg15 sample, and (e) one of the enlarged grains of the Mg15 sample.

is shown. The surface morphology is found different than in the Pure and Mg05 samples. A granular formation is dominant on the surface with different particle sizes. It has been determined from EDS analysis that these particles have predominantly Y-211 and also a little amount of MgO phases.

However, as seen in Fig. 3d, it was found that the structure in the Mg15 sample completely degenerated, and the partially melted structure in the previous substitution levels turned into a mainly granular structure with a few micron sizes and different geometries. At the same time, it is clearly seen that the spaces between the particles begin to form intensively, and the porosity increases (Fig. 3d). In addition, it has been observed that MgO particles of 50nm–5μm in size in different geometries with approximately 96% MgO composition are densely located on the surface together with the Y-123 and Y-211 phases. One of the enlarged grains of the Mg15 sample is shown, as an example, in Fig. 3e, and clearly shows us that MgO does not fully react with the Y-123 matrix. This situation is also confirmed by the XRD analysis in Fig. 1. However, a similar formation was also found, to a lesser extent, in the Mg10 sample. This clearly shows us that the solubility of MgO in the matrix can be possible up to a certain limit (in our case, this limit value is understood to be up to 0.5 Mg substitution) and that the solubility starts to decrease as the substitution rate increases.

3.3. Electrical measurements

The electrical measurement, $\rho(T)$, results of the produced samples, in the temperature range of 300 K and 60 K, and under the applied magnetic field up to 9 T, are given in Fig. 4a–f and Table II, for Pure, Mg05, and Mg10 samples. Since the Mg15 sample showed a very high resistance value both at room temperature and also at 4.2 K and remained well over the measurement limits of the equipment, the measurement could not be performed during this work. The resistivity values of the samples decreased linearly from 300 K to T_c, revealing that electron-phonon scattering is the dominant mechanism in Pure, Mg05 and Mg10 samples. The results obtained for $\rho(T)$ values were fitted to the equation $\rho_n(T) = \rho_o + \alpha T$, and it was found that the residual resistivity of the Mg10 sample was 1.17 times higher than that of the Mg05 sample, and 1.22 times higher than that of the Pure sample. This reveals that the scattering is increased with the increase of Mg concentration in the matrixes due to the disruption of structural order at the atomic scale. Also, this can be associated with the large difference in ionic radius (Ba^{+2} — 1.35 nm vs Mg^{+2} — 0.72 nm), meaning that there will be a significant reorganization in the structure when the Mg concentration is increased, which is also evidenced in XRD patterns.

The $d\rho/dT$ vs T plots of Pure, Mg05, and Mg10 samples are given in Fig. 4d–f. The fact that the curves obtained in the graphs are in the form of a single peak in the phase transition region, indicates that the Y-123 phase is dominant. However, as seen in Fig. 4e and f, the peak widths increase, which is considered an effect of impurity phases in the material, as confirmed in XRD and SEM-EDS analysis, and is interpreted as the effect of scattering from non-conducting phases and also possible dislocations in the material at T_c region.

Hole concentration, p, is known as a significant parameter in terms of superconductivity in YBCO superconductors, and it is important to calculate the number of holes per Cu atom because of the superconducting role of CuO chains/planes in the samples. Accordingly, the following equation was used to find out how the p concentration changed with the Mg substitution

$$\frac{T_c}{T_c^{\max}} = 1 - 82.6\big(p - 0.16\big)^2. \tag{1}$$

In (1) [39–41], p gives the number of holes per Cu and $T_c^{\max}$, is the maximum T_c for the Y-123 system, and is taken as 92 K. The p values calculated for Pure, Mg05, and Mg10 samples were found to be 0.134, 0.136, and 0.139, respectively. Meanwhile, the p-value found for Pure is in agreement with the previously calculated values (0.133–0.135) in the literature [18, 42–45], however, the p-value increases as the Mg substitution increases. This indicates a transfer of the hole concentration of Y-123 material from the optimal-doped region to the over-doped region, and may cause an excessive hole concentration in the Cu–O chain. We assumed that this causes suppression of superconductivity at high Mg concentration cases.

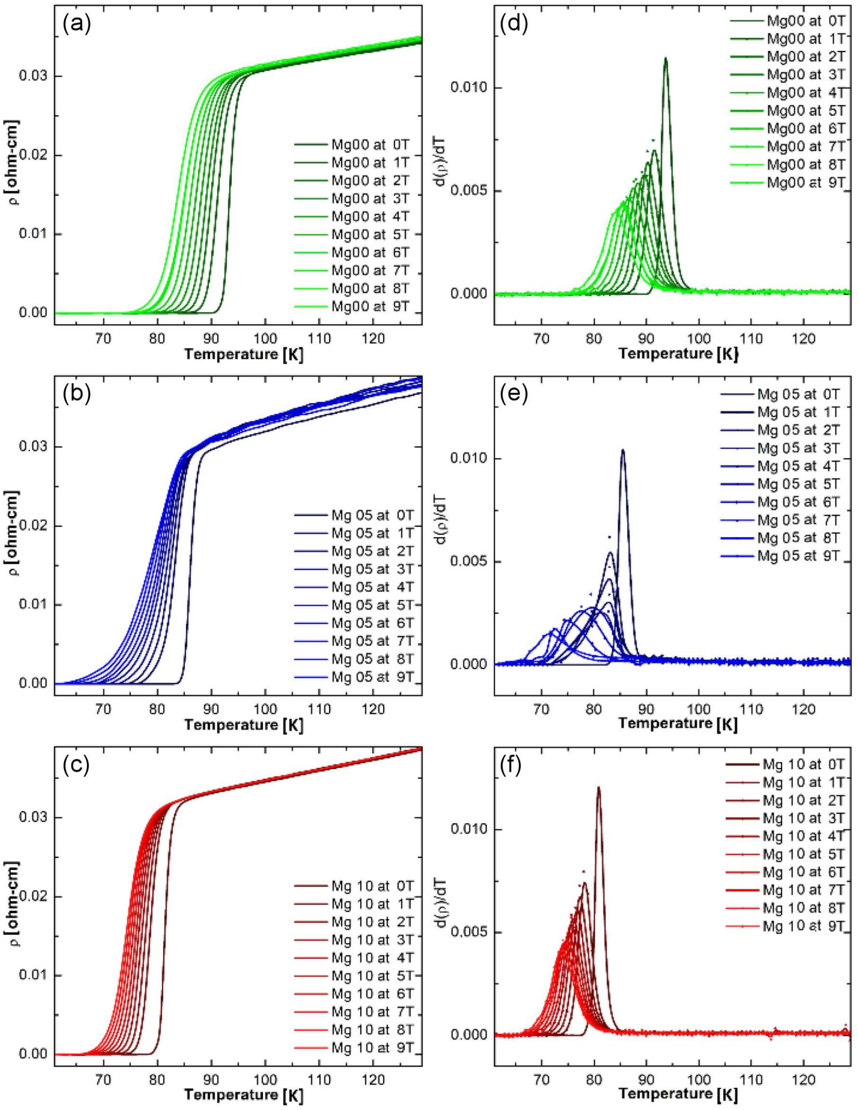

Fig. 4. The graphs of ρ versus T of (a) Pure sample, (b) Mg05 sample, (c) Mg10 sample, and $\mathrm{d}\rho/\mathrm{d}T$ versus T plots of (d) Pure sample, (e) Mg05 sample, and (f) Mg10 sample.

3.4. Activation energy calculations $U(H,T)$

The activation energy, $U(H,T)$, plays a significant role in determining the flux dynamics in HTS systems. With the calculation of $U(H,T)$, important details can be obtained about the height of the energy barrier, which can provide relevant information for vortex mobility. In the thermally activated flux flow (TAFF) regime, the thermally activated resistivity is given by the following equation [46, 47]

$$\rho = \rho_0 \exp\left(-\frac{U(J,H,T)}{k_\mathrm{B}T}\right). \tag{2}$$

In (2), ρ_0 is the pre-exponent factor, k_B is the Boltzman constant, and U is the activation energy depending on temperature (T), current density (J_c), and applied field (H) for the flux motion. For constant current values, the functional dependence of $U(H,T)$ gives correct information for the dissipation mechanism. However, $U(H,T)$ can be thought of as a temperature-independent function in the low resistance regions of the samples for a narrow temperature region, and thus J will be negligibly small under these conditions. Accordingly, the activation energy can be calculated from the slope of the graph of $\ln(\rho/\rho_0)$ relative to $1/T$ as $U(H)$ — depending only on the field. The graphs of $\ln(\rho/\rho_0)$ versus $1/T$ are given in Fig. 5a–c for the samples Pure, Mg05, and Mg10, respectively, and the activation energy values calculated from the slopes of the graphs are given in Fig. 6 and Table III. It was found that the calculated $U(H)$ values for all samples started to decrease with the increase of Mg concentration and magnetic field. In this case, the decrease in $U(H)$ with increasing Mg concentration is related to both flux trapping and flux motion, and it is assumed that especially flux motion slows down, in our case, with the Mg substitution. Similarly, the significant decrease in $U(T)$ with the increase

TABLE II

Electrical transport, pinning force, and activation energy properties of the samples prepared, where $\Delta T = (T_{c,}^{\text{onset}} - T_{\text{zero}})$, and the error is 0.02 %.

H_{app} [T]	T_c^{onset} [K]	T_{zero} [K]	$\Delta T[K]$	Fitting param. α ($\times 10^4$)	Hole number p	J_c^{mag} at 8 K ($\times 10^4$) [A/cm^2]	F_p at 8 K [T.A/cm^2]	U_0 [eV]
				Pure				
0	95.3	91.4	3.9	1.066	0.134	26.7	0	1.64
1	94.2	87.6	6.6	–	–	13.8	1.38×10^9	0.67
2	92.5	85.1	7.4	–	–	10.2	2.04×10^9	0.65
3	91.9	83.6	8.3	–	–	8.80	2.64×10^9	0.54
4	91.3	81.6	9.7	–	–	8.29	3.32×10^9	0.45
5	90.8	79.1	11.1	–	–	8.01	4.01×10^9	0.47
6	89.3	76.8	12.5	–	–	7.87	4.72×10^9	0.4
7	88.7	75.9	12.8	–	–	7.78	5.45×10^9	0.35
8	87.4	73.9	13.5	–	–	7.71	6.17×10^9	0.30
9	86.5	72.2	14.3	–	–	...	...	0.28
				Mg05				
0	95.2	91.0	4.2	1.168	0.136	20.4	0	1.34
1	84.6	76.9	7.7	–	–	10.6	1.06×10^9	0.28
2	83.7	73.8	9.9	–	–	7.76	1.55×10^9	0.25
3	83.1	72.5	10.6	–	–	6.75	2.03×10^9	0.20
4	82.2	71.1	11.1	–	–	6.30	2.52×10^9	0.17
5	81.8	70.2	11.6	–	–	6.08	3.04×10^9	0.17
6	81.5	68.4	13.1	–	–	5.97	3.58×10^9	0.17
7	81.0	67.5	13.5	–	–	5.92	4.14×10^9	0.13
8	80.6	66.5	14.1	–	–	5.88	4.71×10^9	0.13
9	79.9	65.0	14.9	–	–	...	...	0.12
				Mg10				
0	83.9	77.8	6.1	1.417	0.139	5.08	0	1.21
1	80.9	71.7	9.2	–	–	2.37	2.37×10^8	0.58
2	80.5	70.1	10.4	–	–	1.75	3.50×10^8	0.54
3	80.0	69.0	11.0	–	–	1.49	4.48×10^8	0.46
4	79.7	68.0	11.7	–	–	1.35	5.42×10^8	0.39
5	79.2	67.0	12.2	–	–	1.25	6.26×10^8	0.38
6	78.8	65.1	13.7	–	–	1.18	7.10×10^8	0.35
7	78.5	64.0	14.5	–	–	1.13	7.89×10^8	0.31
8	78.1	63.0	15.1	–	–	1.07	8.60×10^8	0.28
9	77.8	61.8	16.0	–	–	...	...	0.24

of Mg concentration is considered to indicate that the point pinning (trapping) characteristic of fluxes starts to be thermally activated on the sample surface, and its tendency to remain motionless increases with the Mg substitution.

3.5. Upper critical field calculations $H_{c2}(0)$

To determine the upper critical field, $H_{c2}(0)$, calculations were made using the Werthamer–Helfand–Hohenberg (WHH) equation and the 10%, 50%, and 90% criteria of the resistivity curve. The WHH equation is as follows [45]

$$H_{c2}\left(0\right) = -0.693 T_c \left(\frac{\mathrm{d}H_{c2}}{\mathrm{d}T}\right)\Big|_{T=T_c}. \qquad (3)$$

According to (3), calculated $H_{c2}(T)$ versus temperature curves of the produced samples are given in Fig. 7. From these curves, the slopes calculated for the Pure sample are −2.545, −2.139, and −1.901; for the Mg05 sample are −3.442, −1.971, and −1.464; and for Mg10 sample are −4.455, −2.084, and −1.061. The calculated values of $H_{c2}(0)$, using slopes and (3), are given in Table III.

In order to control the results obtained with the WHH formula, theoretical H_{c2} values were calculated using the equation developed by Wen et al. [46]. Wen's equation is as follows

$$H_{c2}\left(T\right) = H_{c2}\left(0\right) \tfrac{1-t^2}{1+t^2}, \qquad (4)$$

TABLE III

Calculated H_{c2} values according to WHH and Wen's formula, the error is $\sim 3\%$.

Sample	$H_{c2}(0)$ ρ (90% criteria) [T]		$H_{c2}(0)$ ρ (50% criteria) [T]		$H_{c2}(0)$ ρ (10% criteria) [T]	
	WHH formula	Wen formula	WHH formula	Wen formula	WHH formula	Wen formula
Pure	308	318	179	183	103	107
Mg05	274	281	128	134	75	78
Mg10	109	115	97	99	49	52

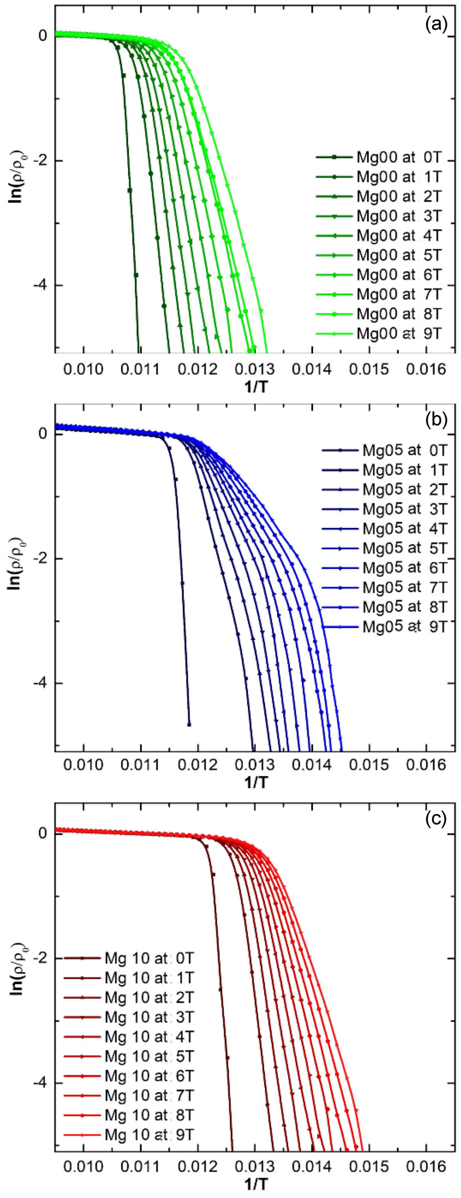

Fig. 5. The graphs of $\ln(\rho/\rho0)$ versus $1/T$ of the Pure, Mg05, and Mg10 samples.

where $t = T/T_c$ is known as reduced temperature. As a result of the calculations made using (4) and the 10%, 50%, and 90% criteria of the resistivity curve, $H_{c2}(0)$ values were found as 318, 183, and 107 T for the Pure sample; as 281, 134, and 78 T for Mg05 sample; and as 115, 99, and 52 T for Mg10 sample (Table III). As can be seen in Table III, the fact that the results of the calculations made with both methods were close to each other, was found to be important in terms of both the compatibility of the experimental results and the accuracy of the methods.

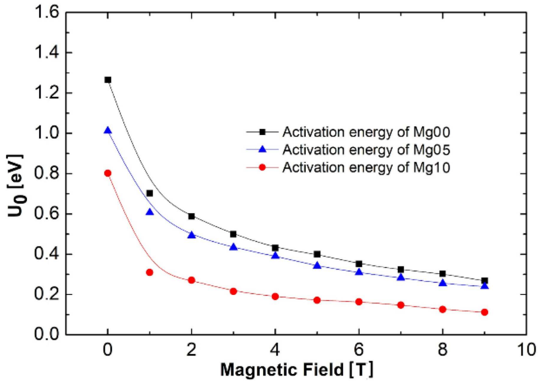

Fig. 6. Calculated activation energy versus applied fields of Pure, Mg05, and Mg10 samples.

As a result, we assume that the decrease of $H_{c2}(0)$ values with increasing Mg concentration is caused by the decrease in the amount of Ba in the structure. Because of the fact that Mg does not completely replace Ba in the crystal structure and remains as a separate phase, the structure turns into a multiphase form, and the formation of Ba vacancies in the structure arises as dislocation centers. In the literature, $H_{c2}(T)$ values in the Y-123 system give quite different results on whether the applied field is perpendicular or parallel to the CuO plane. However, suppression of superconductivity in both cases reveals the possibility of different mechanisms. For example, the quench of superconductivity for cases where H is perpendicular to the CuO_2 plane ($H \perp CuO_2$) can be explained by the orbital effect [48], whereas for the cases where H is parallel to the CuO_2 plane ($B \| CuO_2$) spin–orbit and Zeeman effect can be the effective mechanism [48].

However, it is known from the literature that for $H \perp CuO_2$, the H_{c2} was calculated to be ~ 120 T, whereas $H \| CuO_2$ results are calculated to be at a little over 450 T, especially at low temperatures for undoped Y-123 systems [27, 29, 49]. However, it is known that the nature of the samples, such as single crystal or polycrystalline, also affects the behavior of the material against the applied field. Therefore, considering that the crystals may be oriented

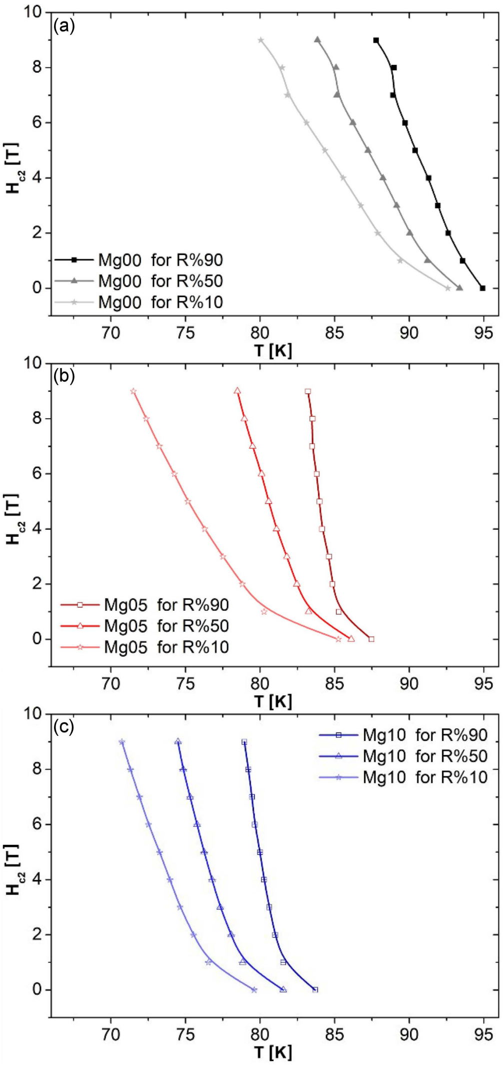

Fig. 7. Upper critical field calculation results using (3), (a) Pure, (b) Mg05, and (c) Mg10 samples.

in different directions in polycrystalline samples, the calculated H_{c2} value is accepted as a mixed case of both $H \perp \mathrm{CuO_2}$ and $H || \mathrm{CuO_2}$ orientations.

In addition to these findings, it was evaluated that the $H_{c2}(T)$ values calculated for the samples were found to be above the BCS paramagnetic limit, $H_P^{\mathrm{BCS}} = 1.84T_c$, and therefore the samples could be considered of unconventional nature.

The characteristic coherence length, $\xi(0)$, of the produced samples was calculated using the $H_{c2}(0)$ values of the samples and the Ginzburg–Landau (GL) equation. Here, the GL equation is given as

$$\xi(0) = \sqrt{\frac{\phi_0}{2H_{c2}(0)}}, \tag{5}$$

where ϕ_0 is the flux quanta. The calculated $\xi(0)$ values are given in Table IV. According to these results, the $\xi(0)$ value was found to be similar to the values previously calculated in the literature for the Y-123 pure sample [25]. However, it is seen that $\xi(0)$ values decrease with the increase of Mg concentration in the matrix. For this reason, we assume that the flux motion, formed in the samples, slows down with the amount of substitution, and the pinning centers are then believed to be localized.

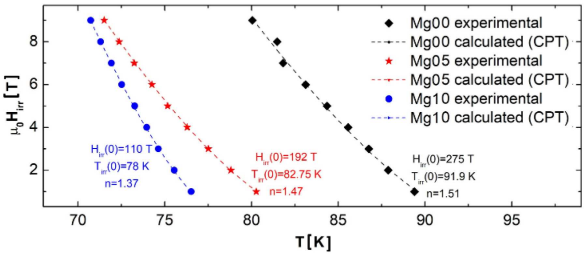

Fig. 8. The plots of H_{irr} fitting curve of the Pure, Mg05, and Mg10 samples.

TABLE IV

The calculated $\xi(0)$ values for the samples prepared.

Sample	$\xi(0)$ [nm]
Pure	0.925
Mg05	0.817
Mg10	0.801

3.6. Irreversibility field $H_{irr}(0)$

The temperature dependence equation of magnetic irreversibility according to collective pinning theory (CPT) is generally given as [27, 52]

$$H_{irr} = H_0 \left(1 - \frac{T_{irr}(H)}{T_{irr}(0)}\right)^n. \tag{6}$$

Magneto-resistance measurement results and (6) were used for the irreversibility-field $\mu_0 H_{irr}(0)$ calculations of the prepared samples, except Mg15. In (6), $T_{irr}(H)$ is the irreversibility temperature under different applied magnetic fields, $T_{irr}(0)$ is the irreversibility temperature under zero applied field, and $T_{irr}(H)/T_{irr}(0)$ is called reduced temperature. Note that H_0, n, and $T_{irr}(0)$ are fitting parameters and are solved by the simple equation as $y = ax^b$. The H_{irr} fitting curve, calculated according to the values of H_0, n, and $T_{irr}(0)$ are given in Fig. 8, and numerical values are given in Table V. The n values for Pure, Mg05, and Mg10 samples were found as 1.51 ± 0.07, 1.47 ± 0.09, and 1.37 ± 0.08, respectively. It is seen that the average value is $n = 1.45 \pm 0.09$, which shows us that the samples can be fitted properly with the giant flux creep (GFC) model [27, 50]. As can be seen, these results are in agreement with the results found in the literature by different groups, especially for polycrystalline YBCO superconductors [27, 50–53]. Calculated $\mu_0 H_{irr}(0)$ values were found to be 275, 192, and 110 T for Pure, Mg05, and Mg10 samples, respectively. According to these results, an unbalanced structure emerges due to the Mg substitution in the Y-123 structure by creating impurities

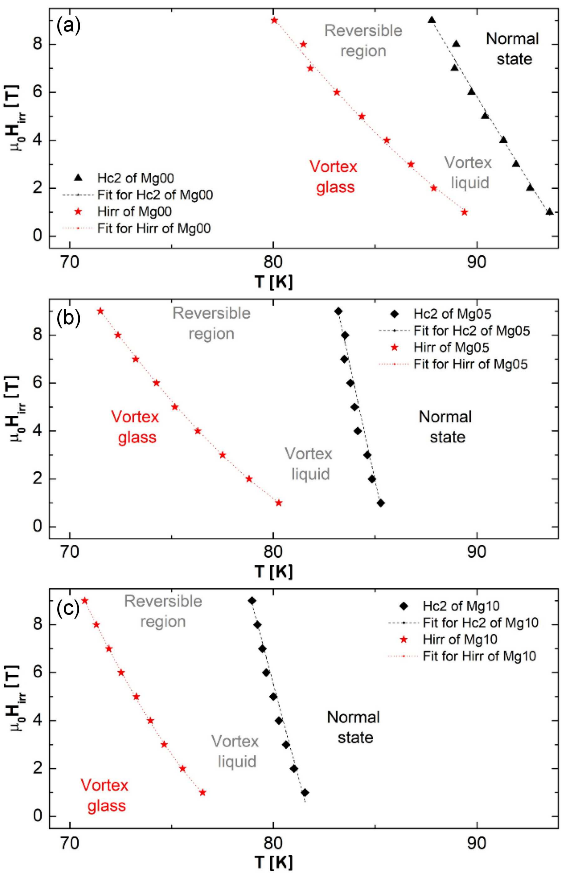

Fig. 9. The plots of the normal state, vortex-liquid, irreversibility line, and vortex-glass region of the Pure, Mg05, and Mg10 samples.

TABLE V

H_{irr} and fitting parameters for the samples prepared.

Sample	$H_{irr}(0)$ [T]	$T_{irr}(0)$ [K]	n
Pure	275	91.9	1.51 ± 0.07
Mg05	192	82.75	1.47 ± 0.09
Mg10	110	78	1.37 ± 0.08

and lattice defects and weakening the grain coupling. Here, if we assume that the pinning centers are formed by the impurities, the lattice defects will then show a random distribution and restrict the movement by pulling the vortex lines and placing them in a point form.

The normal state, vortex-liquid, irreversibility line, and vortex-glass graphs calculated from magnetoresistivity measurement results for Pure, Mg05, and Mg10 samples are given in Fig. 9. According to these results, the Pure sample has a narrower liquid-vortex gap, and this gap is wider in other substituted samples. It is assumed that the irregular structure, formed as a result of Mg substitution, supports the formation of vortex-glass. At low temperatures, the energy of the vortexes is low and stable — due to the pining points, the vortexes trying to attract each other will weaken the thermal fluctuations significantly. On the other hand, at high temperatures (around $T = T_{irr}$), the vortex-glass structure will deteriorate, and as a result, a liquid vortex state will occur. This shows us that the pinning centers are weakened in Mg substitution samples.

3.7. Magnetic characterizations M–H

Magnetization versus applied field (M–H) measurements performed under ±9 T at 8, 10, 20, and 30 K for Pure, Mg05, Mg10, and Mg15 samples are given in Fig. 10a–d. According to M–H measurement, it was observed that the Pure, Mg05, and Mg10 samples had the diamagnetic character for all measured temperatures and exhibited typical superconducting M–H curves, whereas there was no hysteresis in the Mg15 sample. It is seen that the obtained M–H curves have a slightly asymmetrical structure, except for the Pure sample, and this peculiarity becomes more explicit with the increase of Mg concentration in the structure. This is considered to be a result of increased paramagnetism due to impurity phases that are forming in the structure with the Mg substitution.

3.8. Critical current density measurements J_c^{mag}

The magnetization-dependent critical current densities, J_c^{mag}, of the produced samples, except for Mg15, were calculated using Bean's method [53], and the results obtained are given in Fig. 11a–d. According to Bean's method [51], J_c^{mag} can be calculated with the following formula

$$J_c^{mag} = \frac{20\Delta M}{a\left(1 - \frac{a}{3b}\right)}, \tag{7}$$

where a and b are the dimensions of the cross-sectional area of the rectangular-shaped sample ($a < b$ [cm]) and $\Delta M = M^+ - M^-$ [emu] is known as the hysteresis width. According to calculations, the best result was obtained in the Pure sample under zero field and at 8 K as 2.5×10^5 A/cm^2 (Table II). For the Mg05 and Mg10 samples under zero-field and at 8 K, respective values of 2.04×10^5 A/cm^2 and 5.08×10^4 A/cm^2 were obtained. It was found that the J_c^{mag} values of the samples decreased gradually with Mg substitution (Fig. 11a–d). It is clearly seen that there is a 1.25-fold difference between the Pure and the Mg05 sample, and a 4-fold difference between the Mg05 and Mg10 sample. However, despite all these findings, it was observed that the J_c^{mag} values of the samples have not completely or partially disappeared, even under 9 T and at 30 K, and followed a horizontal course with a small slope (Fig. 11a–d). This shows us that the impurity phases and also the resulting structural deformations in the matrix are probably acting as pinning centers in some way. This situation reveals that the structure has a bulk superconducting nature.

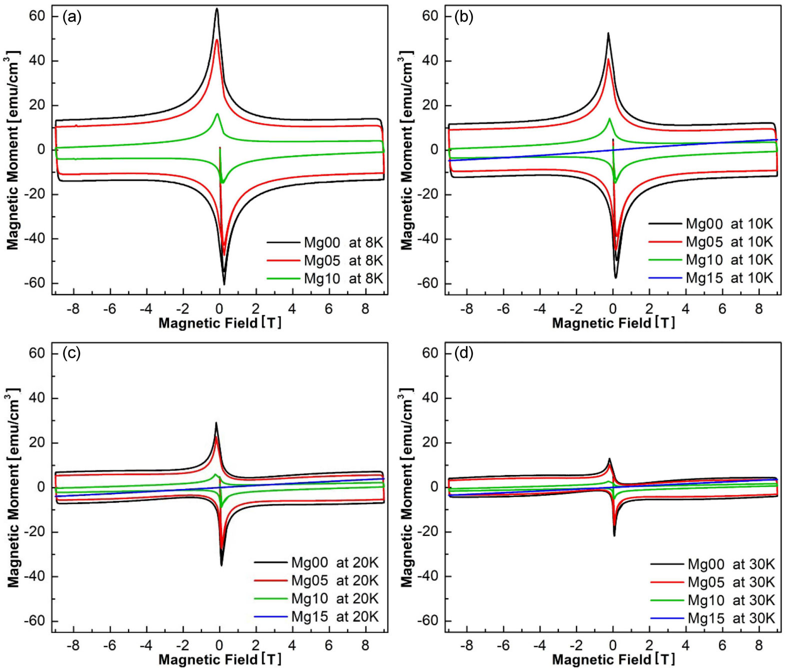

Fig. 10. Magnetic hysteresis loops of the Pure, Mg05, Mg10, and Mg15 samples at (a) 8 K, (b) 10 K, (c) 20 K, and (d) 30 K.

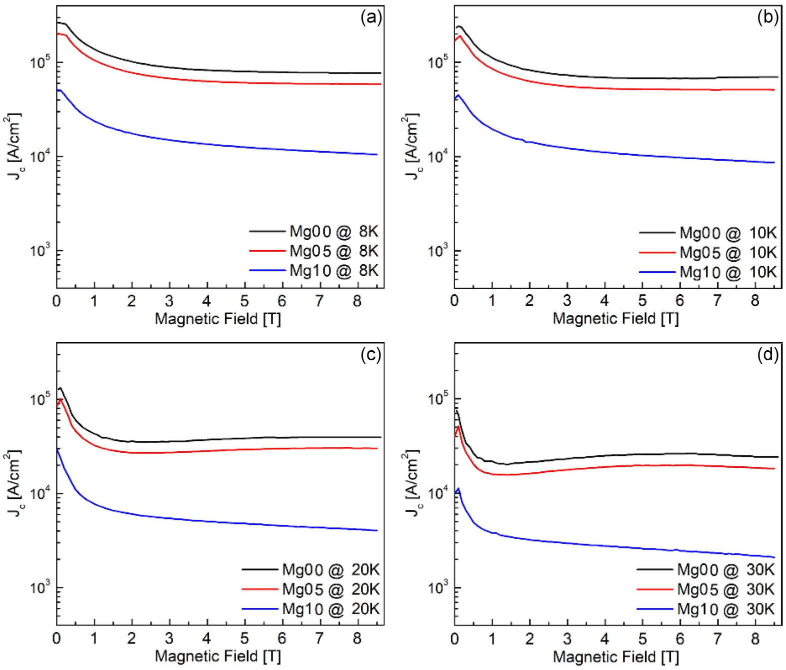

Fig. 11. Calculated J_c^{mag} values of the Pure, Mg05, and Mg10 samples at (a) 8 K, (b) 10 K, (c) 20 K, and (d) 30 K.

3.9. Pinning force calculations F_{p}

In superconducting samples, one of the factors affecting, in particular, the current density is the pinning force, F_{p}. In order to see the change in pinning force with the substitution ratio, the normalized vortex pinning forces of the produced samples ($f_N = F_{\mathrm{p}}/F_{\mathrm{p}}^{\max}$) were calculated as the function of $h = H/H_{irr}$. Here, H_{irr} is defined as the irreversibility field, and in its most general form, it is obtained by linear extrapolation of the $J_c^{1/2}$–H curves to the zero value of J_c and $F_{\mathrm{p}}^{\max}$ is the maximum value of the pinning force [52]. The calculated

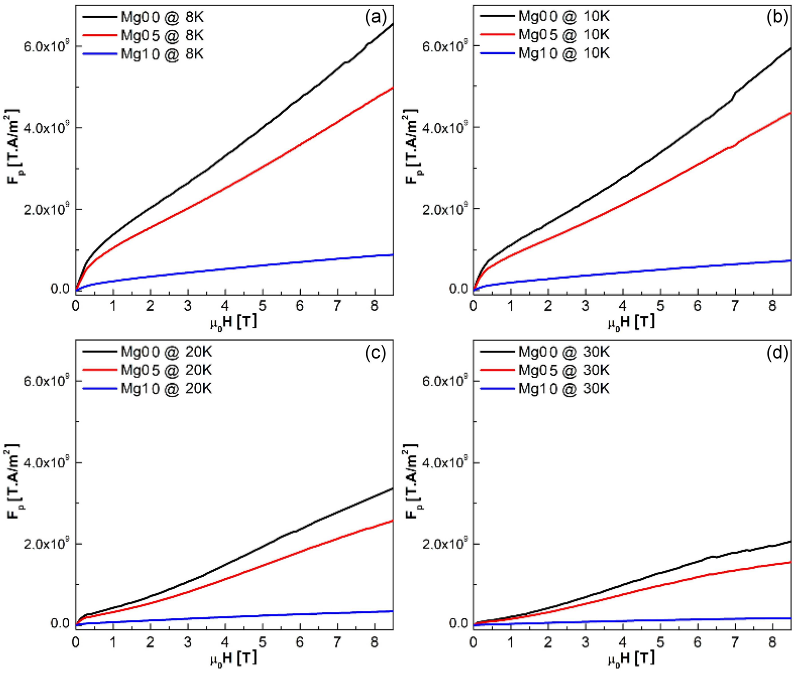

Fig. 12. Calculated pinning force at (a) 8 K, (b) 10 K, (c) 20 K, and (d) 30 K for Pure, Mg05, and Mg10 samples.

pinning forces of the samples are given in Fig. 12a–d. However, despite the 9 T maximum field measurement limit, it is seen that the F_p value is constantly increasing, and it cannot be predicted where exactly this increase will end or where the maximum will be (Fig. 12). For all that, according to the Dew–Hughes model, for unconventional superconductors and small-size surface pinning mechanisms, h_max is known as 0.33 [52, 53]. In this case, since h_max could not be determined for any of our samples, we assume that it may approach 0.33. Accordingly, it is accepted that small pinning centers are formed on the surface of the samples in point form, and assumed that this creates a reasonable critical current density and pinning force even in the Mg10 substituted samples.

4. Conclusion

In this study, the results of Y-123 superconducting samples with the nominal composition of $\mathrm{Y(Ba_{1-x}Mg_x)2Cu_3O_{7-\delta}}$, where $x = 0.0$ 0.5, 1.0, and 1.5, were prepared by the solid-state method and structural, electrical and magnetization analyzes and presented. It was observed that the crystal parameters of Y-123 were changed by the substitution of Mg instead of Ba, but there was no deviation from the orthorhombic symmetry. Y-211 and MgO impurity phases were formed together with the Mg substitution, and they became the dominant phase in high substitution ratios. It was also found that Mg did not dissolve in Y-123 and remained as a separate phase with $\sim 96\%$ purity up to a certain limit. The superconducting properties of the samples started to deteriorate with the substitution and were completely destroyed at the substitution ratio of $x = 1.5$. In addition, it was observed that there was a significant increase in hole concentration with substitution, and the samples shifted from the optimally-doped region to the over-doped region.

Moreover, it was found that the calculated $U(H)$ values started to decrease with the Mg concentration and magnetic field. We assumed that the decrease in $U(H)$ is related to both flux trapping and flux motion, and it is also assumed that, in our case, especially flux motion slows down with the Mg substitution. It is also considered that it will be possible to interpret the obtained results within the framework of non-magnetic impurity scattering effects in d-wave superconductors.

Acknowledgments

Ö.Ç. and K.Y. thank Prof. Dr. M.E. YAKINCI for allowing us to use his experimental setup and for his valuable comments on magnetization analysis.

References

[1] A.N. Kamarudin, M.M.A. Kechik, S.N. Abdullah et al., *Coatings* **12**, 91 (2022).

[2] L. Wang, L. Shen, Y. Li, Y. Wang, Y. Xiao, X. Zhang, F. Xu, X. Hu, *Acta Metall. Sin. (Engl. Lett.)* **35**, 67 (2022).

[3] P. Prayoonphokkharat, P. Amonpattaratkit, A. Kosuga, A. Watcharapasorn, *J. Alloys Compd.* **871**, 159552 (2021).

[4] M. Başoğlu, İ. Düzgün, A. Öztürk, *J. Supercond. Novel Magn.* **34**, 1077 (2021).

[5] Ö. Çi˙çek, K. Yakinci, *J. Mol. Struct.* **1211**, 128089 (2020).

[6] E. Hannachi, M.A. Almessiere, Y. Slimani, A. Baykal, F. Ben Azzouz, *J. Alloys Compd.* **812**, 152150 (2020).

[7] O. Ozturk, A.R.A. Nefrow, F. Bulut, H. Ada, M.B. Turkoz, G. Yildirim, *J. Mater. Sci. Mater. Electron.* **31**, 7630 (2020).

[8] Y. Slimani, E. Hannachi, A. Ekicibil, M.A. Almessiere, F. Ben Azzouz, *J. Alloys Compd.* **781**, 664 (2019).

[9] M. Malmivirta, H. Rijckaert, V. Paasonen, H. Huhtinen, T. Hynninen, R. Jha, V.P.S. Awana, I. Van Driessche, P. Paturi, *Sci. Rep.* **7**, 14682 (2017).

[10] T. Kabutoya, M. Koshimizu, Y. Fujimoto, K. Asai, *Sens. Mater.* **20**, 10 (2017).

[11] Y.A. Opata, J.F.H.L. Monteiro, A.R. Jurelo, E.C. Siqueira, *Physica C* **549**, 107 (2018).

[12] D.M. Gokhfeld, S.V. Semenov, I.V. Nemtsev, I.S. Yakimov, D.A. Balaev, *J. Supercond. Novel Magn.* **35**, 2679 (2022).

[13] L. Jansen, R. Block, *Physica A* **277**, 183 (2000).

[14] V. Sandu, E. Cimpoiasu, T. Katuwal, S. Li, M.B. Maple, C.C. Almasan, *Phys. Rev. Lett.* **93**, 177005 (2004).

[15] H. Shakeripour, S.S. Hosseini, S.S. Ghotb, B. Hadi-Sichani, S. Pourasad, *Ceram. Int.* **47**, 8 (2021).

[16] A.R. Hamoudi, A. May, A. Henniche, J.H. Ouyang, A. Guillet, *Ceram. Int.* **47**, 18 (2021).

[17] U. Erdem, M. B. Turkoz, G. Yıldırım, Y. Zalaoglu, S. Nezir, *J. Alloys Compd.* **884**, 161131 (2021).

[18] A. Los, B. Dabrowski, K. Rogacki, *Curr. Appl. Phys.* **27**, 1 (2021).

[19] S. Attaf, M. F. Mosbah, R. Fittipaldi, D. Zola, S. Pace, A. Vecchione, *Physica C* **477**, 36 (2012).

[20] V. N. Vieira, P. Pureur, J. Schaf, *Phys. Rev. B* **66**, 224506 (2002).

[21] J. Figueras, T. Puig, A.E. Carrillo, X. Abradors, *Supercond. Sci. Technol.* **13**, 1067 (2000).

[22] L. Raffo, R. Caciuffo, D. Rinaldi, F. Licci, *Supercond. Sci. Technol.* **8**, 409 (1995).

[23] A. Vyas, C.C. Lam, L.J. Shen, *Physica C* **341–348**, 2 (2000).

[24] M.A. Aksan, M.E. Yakinci, *J. Alloys Compd.* **385**, 1 (2004).

[25] E. Hannachi, Y. Slimani, A. Ekicibil, A. Manikandan, F. Ben Azzouz, *J. Mater. Sci. Mater. Electron.* **30**, 8805 (2019).

[26] G. Grissonnanche, O. Cyr-Choinière, F. Laliberté et al., *Nat. Commun.* **5**, 3280 (2014).

[27] Z. Hao, Y. Wu, Y. Enomoto, K. Tanabe, N. Koshizuka, *J. Appl. Phys.* **91**, 9251 (2002).

[28] S.H. Hong, H. Xu, E. Gao, S. Sahba, Q.Y. Ma, *IEEE Trans. Appl. Supercond.* **9**, 2 (1999).

[29] J.L. Smith, J.S. Brooks, C.M. Fowler et al., *J. Supercond.* **7**, 269 (1994).

[30] M.A. Aksan, M.E. Yakinci, K. Kadowaki, *J. Supercond. Novel Magn.* **23**, 371 (2010).

[31] R. Algarni, Y. Slimani, E. Hannachi, M.A. Almessiere, B.H. Alqahtani, S. Akhtar, F. Ben Azzouz, *Curr. Appl. Phys.* **27**, 89 (2021).

[32] M.A. Almessiere, Y. Slimani, E. Hannachi, R. Algarni, F. Ben Azzouz, *J. Mater. Sci. Mater. Electron.* **30**, 17572 (2019).

[33] Crystallography Open Database.

[34] B. Sahoo, A.K. Singh, D. Behera, *Mater. Chem. Phys.* **240**, 122252 (2020).

[35] S. Chamekh, A. Bouabellou, *Adv. Chem. Eng. Sci.* **8**, 1 (2018).

[36] R. Rangel, D.H. Galván, G.A. Hirata, E. Adem, F. Morales, M.B. Maple, *Supercond. Sci. Technol.* **12**, 264 (1999).

[37] A. Kujur, D. Behera, *J. Magn. Magn. Mater.* **12**, 264 (2015).

[38] B. A. Malik, K. Asokan, V. Ganesan, D. Singh, M.A. Malik, *Physica C* **531**, 85 (2016).

[39] M.R. Presland, J.L. Tallon, R.G. Buckley, R.S. Liu, N.E. Flower, *Physica C* **176**, 1 (1991).

[40] R. Terzioglu, *J. Mater. Sci. Mater. Electron.* **32**, 4737 (2021).

[41] S. Altin, M.A. Aksan, Y. Balci, M.E. Yakinci, *J. Supercond. Novel Magn.* **22**, 775 (2009).

[42] E.F. Talantsev, S.C. Wimbush, N.M. Strickland, J.A. Xia, P. D'Souza, J.G. Storey, J.L. Tallon, B. Ingham, R. Knibbe, N.J. Long, *IEEE Trans. Appl. Supercond.* **23**, 7200205 (2013).

[43] P.H. Kes, J. Aarts, J. Vanden Berg, C.J. Van der Beek, J.A. Mydosh, *Sci. Technol.* **1**, 5 (1989).

[44] H.L. Li, K.Q. Ruan, S.Y. Li, Y. Yu, C.Y. Wang, L.Z Cao, *Physica C* **386**, 560 (2003).

[45] N.R. Werthamer, E. Helfand, P.C. Hohenberg, *Phys. Rev.* **147**, 295 (1966).

[46] J. Wen, G. Xu, Z. Xu, Z.W. Lin, Q. Li, W. Ratcliff, G. Gu, M. Tranquada, *Phys. Rev. B* **80**, 104506 (2009).

[47] G. Grissonnanche, O. Cyr-Choinière, F. Laliberté et al., *Nat. Commun.* **5**, 3280 (2014).

[48] M. Rekaby, R. Awad, A.I. Abou-Aly, M. Yousry, *J. Supercond. Novel Magn.* **32**, 3483 (2019).

[49] A. Hamrita, Y. Slimani, M.K.B. Salem, E. Hannachi, L. Bessais, F.B. Azzouz, M.B. Salem, *Ceram. Int.* **40**, 1 (2014).

[50] F.M. Barros, F.W. Fabris, P. Pureur, J. Schaf, V.N. Vieira, A.R. Jurelo, M.P. Cantão, *Phys. Rev. B* **73**, 094515 (2006).

[51] C.P. Bean, *Rev. Mod. Phys.* **36**, 31 (1964).

[52] K. Onar, B. Ozçelik, N.K. Güler, H. Okazaki, H. Takeya, Y. Takano, M.E. Yakinci, *J. Alloys Compd.* **683**, 164 (2016).

[53] C.S. Yadav, P.L. Paulose, *Solid State Commun.* **151**, 3 (2011).